Accepted Article

This manuscript has been accepted after peer review and appears as an Accepted Article online prior to editing, proofing, and formal publication of the final Version of Record (VoR). This work is currently citable by using the Digital Object Identifier (DOI) given below. The VoR will be published online in Early View as soon as possible and may be different to this Accepted Article as a result of editing. Readers should obtain the VoR from the journal website shown below when it is published to ensure accuracy of information. The authors are responsible for the content of this Accepted Article.

FULL PAPER

Acetic acid ketonization over Fe₃O₄/SiO₂ for pyrolysis bio-oil upgrading

James A. Bennett,[a] Christopher M.A. Parlett,[a] Mark A. Isaacs,[a] Lee J. Durndell,[a] Luca Olivi,[b] Adam F. Lee*[a] and Karen Wilson*[a]

Abstract: A family of silica supported, magnetite nanoparticle catalysts was synthesized and investigated for continuous flow acetic acid ketonization as a model pyrolysis bio-oil upgrading reaction. Physicochemical properties of Fe₃O₄/SiO₂ catalysts were characterized by HRTEM, XAS, XPS, DRIFTS, TGA and porosimetry. Acid site densities were inversely proportional to Fe₃O₄ particle size, although acid strength and Lewis character were size invariant, and correlated with the specific activity for vapor phase acetic ketonization to acetone. A constant activation energy (~110 kJ.mol^{-1}), turnover frequency (~13 h^{-1}) and selectivity to acetone of 60 % were observed for ketonization across the catalyst series, implicating Fe₃O₄ as the principal active component of Red Mud waste.

Introduction

Bio-oil is a renewable (and potentially sustainable) liquid fuel prepared by pyrolysis of biomass feedstocks such as agricultural or forestry waste, energy crops, or microalgae solid residues and sewage sludge.[1] Direct use of unprocessed fast pyrolysis bio-oils is hindered by undesirable physicochemical properties, including a low heating value due its high oxygen content, high viscosity, and high acidity which renders it corrosive and (thermo)chemically unstable.[2] The latter arises from the presence of significant concentrations of carboxylic acids formed during the thermal decomposition of cellulose and hemicellulose biomass components, with acetic acid at levels between 1-10 %. Heterogeneous catalysis affords several routes to the upgrading of pyrolysis bio-oils, including esterification,[3] aldol condensation,[4] hydrodeoxygenation (HDO),[5] and ketonization,[6] each offering advantages and drawbacks. Esterification of bio-oil condensates over solid Brönsted acids can afford low temperature liquid phase upgrading of the aqueous bio-oil fraction,[7] but requires a sustainable alcohol source (although self-esterification with phenolic bio-oil components is possible) and only slightly lowers the oxygen content. Aldol condensation over solid bases enables chain

growth and improves oil stability by removing reactive oxygenate components, but does not neutralise the intrinsic acidity which indeed induces catalyst deactivation. Hydrodeoxygenation is an effective means to obtain cyclic and aliphatic alkanes as drop-in transportation bio-fuels, however this requires a sustainable source of molecular hydrogen, while the metal component of HDO catalysts is susceptible to leaching in acidic bio-oils and hence their neutralisation should help minimise precious metal usage. Ketonization, through the condensation of two carboxylic acid molecules to form a heavier ketone while eliminating CO_2 and water (Scheme 1), affords a facile means to simultaneously reduce the acidity and oxygen content of pyrolysis vapor (through close-coupling to a pyrolysis unit) or associated bio-oil condensate. For a monocarboxylic acid (RCOOH) such as acetic acid, ketonization lowers the oxygen content by 75 % and increases the chain length by (R-1) carbon atoms.

Metal oxides have been widely demonstrated as active catalysts for ketonization,[8] including iron oxides[9] which are a major component of Red Mud. Red Mud is an industrial waste material from bauxite mining for aluminium production,[10] and comprises a toxic and caustic mixture of transition, alkali and alkali earth metal oxides. Such waste is generally sent to landfill, and hence in conjunction with the scale (120 million tons per annum) of this hazardous material production, additional opportunities are sought to add value to Red Mud waste streams.[11] Consequently, there are several literature reports of potential processes addressing the valorisation of Red Mud, including its use in construction,[12] wastewater treatment,[13] preparation of geopolymers[14] and magnetic materials,[15] energy storage[16] and catalysis for diverse transformations such as biodiesel production[17], biomass pyrolysis,[18] oxidation[19] and hydrogen production.[20] and the upgrading of fast pyrolysis bio-oils.[21] Hematite, α-Fe₂O₃, is a major catalytically active component of Red Mud, constituting typically 30-50 wt%,[22] and has been investigated for the ketonization of formic and acetic acid mixtures as model reactions for upgrading of pyrolysis bio-oils. Hematite present in Red Mud is reported to reduce to ferromagnetic Fe₃O₄ during reaction >350 °C.[21] This reduced mixture is itself catalytically active, but exhibits superior selectivity to the parent Red Mud with 10-20 % higher ketone selectivity.[21-22] Acetic acid ketonization over bulk hematite is also reported to induce in situ catalyst reduction to Fe₃O₄, which is proposed to exhibit superior activity to Fe₂O₃.[23] Indeed, Taimoor et al report that Fe₂O₃ ketonization activity in enhanced upon the addition of 50 vol% H₂ to the feedstream,[9] although direct evidence for Fe₃O₄ formation was not provided. Nevertheless, the literature consensus is that magnetite is probably the stable, and catalytically active, iron oxide phase present during ketonization.

[a]   Dr. J.A. Bennett, Dr. C.M.A. Parlett, Dr. M.A. Isaacs, Dr. L.J. Durndell, Prof. A.F. Lee, Prof. K. Wilson
European Bioenergy Research Institute
Aston University
Birmingham, B4 7ET (UK)
E-mail: k.wilson@aston.ac.uk
[b]   Dr L. Olivi
Sincrotrone TriesteTrieste
34012 Basovizza (Italy)

Supporting information for this article is given via a link at the end of the document.

The mechanism(s) of heterogeneously catalysed carboxylic acid ketonization, and associated rate-determining step(s) have yet to be unequivocally established,[6, 24] with a range of reactive intermediates, such as ketenes, enols, acyl carbonium ions, acid anhydrides and β-ketoacids invoked. However, there is agreement that adsorbed carboxylate ions are required, and an α-hydrogen must be present on at least one of the reacting acid functions.[24a, 25] The barrier to abstraction of the latter α-hydrogen by lattice oxygen over a monoclinic $ZrO_2(111)$ surface is calculated by DFT as between 120-159 $kJ.mol^{-1}$, depending on the degree of branching at the α-carbon,[26] similar to the experimentally derived activation energy for acetic acid ketonization over ZrO_2 of 117 $kJ.mol^{-1}$.[25b] This correlation suggests that α-hydrogen abstraction may be rate-determining, as proposed for acid ketonization over CeO_2[27] and TiO_2.[28] However, condensation and decarboxylation steps have also been proposed to be limiting,[25b] with evidence for a bimolecular rate-determining step in which adsorbed carboxylate is attacked by enolate to form a β-ketoacid intermediate.[29] These mechanisms generally invoke the dissociative adsorption of a carboxylic acid as a carboxylate over a Lewis acid site, with the carboxylate conjugate proton bound at a neighbouring lattice oxygen Lewis base site. A second Lewis acid center adjacent to the first is also proposed for activation of the second carboxylic acid molecule and their subsequent coupling. Carboxylic acid ketonization is reviewed extensively elsewhere.[6]

The dimensions of Fe_3O_4 nanoparticles are well-known to affect their magnetic,[30] electrical,[31] and rheological[32] properties and photoactivity.[33] However, size effects have never been investigated in iron oxide catalyzed ketonization. Here we explore structure-reactivity relations for the vapor phase ketonization of acetic acid over silica supported magnetite nanoparticles in continuous flow.

Results and Discussion

A family of Fe_3O_4 catalysts of varying particle size was prepared by dispersing iron oxide over fumed silica at different loadings and characterized by bulk and surface analyses. XRD patterns exhibited reflections characteristic of magnetite crystallites in all cases (Figure 1, JCPDS #75-0033), with peak intensities and widths increasing and decreasing respectively with Fe_3O_4 loading (the weak, broad reflection centered around 21 ° arises from the fumed silica support). Peakwidth analysis using the Scherrer equation revealed a continuous increase in the volume-averaged Fe_3O_4 crystallite diameters from 6 to 45 nm across the family (Table 1), consistent with the corresponding mean particle sizes determined from TEM (Table 1 and Figure S1); TEM also showed a similar, quasi-spherical morphology for the magnetite particles independent of iron oxide loading (Figure S1). Nitrogen porosimetry evidenced type II isotherms indicative of microporous fumed silicas[34] for all materials (Figure S2), whose BET surface areas decreased monotonically with Fe_3O_4 loading (Table 1) presumably associated with micropore blockage. Acid site densities of the materials were proportional to their estimated Fe_3O_4 surface areas (shown in Table S1) calculated

assuming spherical particles with diameters from XRD (Table 1), which reveal a maximum for 28 wt% Fe_3O_4 reflecting the balance between the competing influence of Fe_3O_4 loading and particle size on associated surface area and hence acid density.

Since magnetite and maghemite (γ-Fe_2O_3) are both inverse spinel structures with similar diffraction patterns and d-spacings, confirmation of the supported iron oxide phase sought from X-ray absorption spectroscopy (XAS). The common iron oxide phases (α-Fe_2O_3, γ-Fe_2O_3, Fe_3O_4 and FeO) all exhibit similar, but readily distinguishable K-edge X-ray absorption near edge structure (XANES),[35] with characteristic pre-edge and shoulder features due to 1s→4s and 1s→3d transitions respectively.
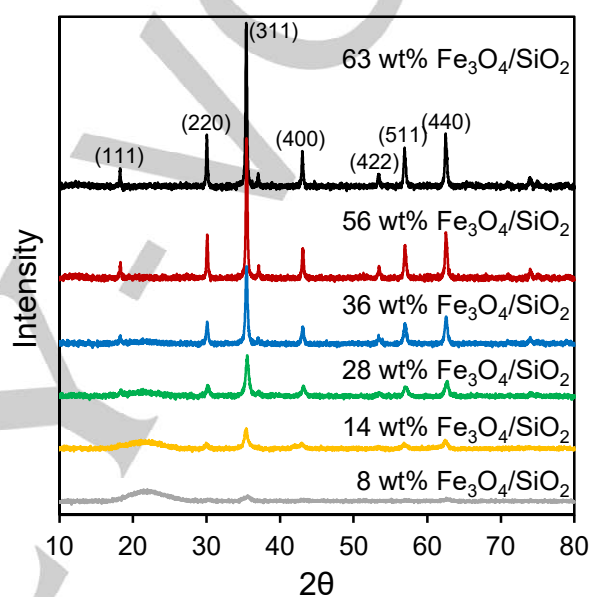

Figure 1. XRD patterns of Fe_3O_4/SiO_2 as a function of Fe loading.

Table 1. Physicochemical properties of Fe_3O_4/SiO_2 catalysts.

Catalyst[a]	Particle size / nm	Surface area[d] / $m^2.g^{-1}$	Acid densi
Fumed SiO_2	-	280	-
4.0 wt% Fe_3O_4/SiO_2	6.1[b] (6.0[c])	225	0.169
8.1 wt% Fe_3O_4/SiO_2	9.7 (11.0)	234	0.199
14.4 wt% Fe_3O_4/SiO_2	16.6 (16.6)	218	0.256
28.0 wt% Fe_3O_4/SiO_2	18.1 (17.0)	207	0.288
36.3 wt% Fe_3O_4/SiO_2	27.8 (27.0)	153	0.220
55.9 wt% Fe_3O_4/SiO_2	38.9 (40.0)	124	0.251
63.4 wt% Fe_3O_4/SiO_2	44.7 (46.0)	103	0.252

[a] Fe loadings from ICP-OES. [b] XRD. [c] HRTEM. [d] BET. [e] Propylamine TGA-MS.

The shape, position and intensity of these features, and the absorption edge (white line), are influenced by site geometry, oxidation state and bondlength, with higher oxidation states shifting absorption features to higher energy; for Fe^{3+} and Fe^{2+} in similar environments this shift is ~2-3 eV,[35a, 36] with the K-edge white line increasing in the order $FeO < Fe_3O_4 < Fe_2O_3$ due to a higher 1s electron binding energy and shortening of the Fe-O bond. Normalized XANES spectra of all Fe_3O_4/SiO_2 materials closely resembled that of a pure Fe_3O_4 standard (Figure 2), exhibiting common pre-edge, shoulder and white line features at 7113, 7124 and 7129 eV respectively, almost identical to those of pure Fe_3O_4. Linear combination fitting of Fe_3O_4/SiO_2 spectra to FeO, Fe_3O_4, Fe_2O_3 and metallic Fe standards confirmed that at least 75 % of iron oxide in all the supported materials was present as Fe_3O_4 (Figure 2, inset).
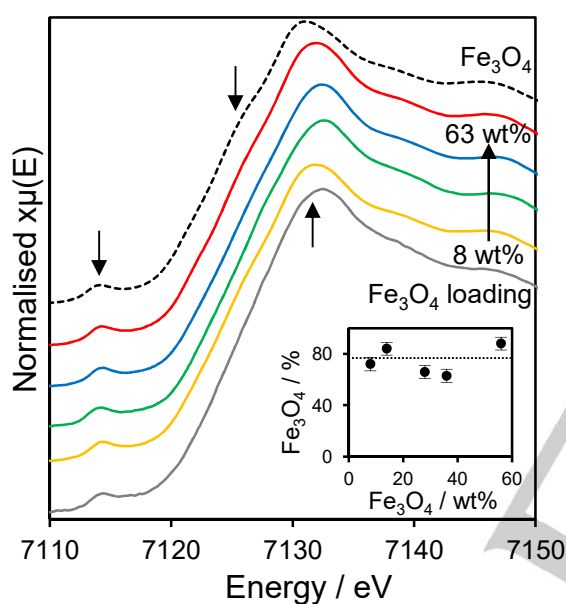

Figure 2. Normalized Fe K-edge transmission XAS of Fe_3O_4/SiO_2 as a function of Fe loading.

The nature of the supported iron oxide phase and it's surface concentration was also studied by XPS (Figure S3). Multiplet splitting, due to crystal field splitting and shake-up processes, strongly influences the 2p XPS spectra of many 3d transition metals;[37] Fe^{3+} and high-spin Fe^{2+} possess unpaired d electrons and hence their 2p XP spectra exhibit multiplet splitting.[37-38] The 2p XP spectra of the present Fe_3O_4/SiO_2 family all exhibited broad $2p_{3/2}$ and $2p_{1/2}$ spin-orbit split multiplets with binding energies centred around 710 eV and 723 eV respectively. Theoretical[37a] and experimental[38a] studies of Fe_3O_4 demonstrate that the $2p_{3/2}$ region requires fitting with 7 components; two arising from high-spin Fe^{2+} and five peaks from Fe^{3+}. Our XP spectra exhibited an excellent fit to the multiplet components of Fe_3O_4 (examplar for 63 wt% Fe_3O_4/SiO_2 is shown in Figure S4), with a fitted $Fe^{3+}:Fe^{2+}$ intensity ratio of 2.08:1 almost identical to that predicted for stoichiometric Fe_3O_4. The same stoichiometry was obtained by fitting the Fe 2p XP spectra
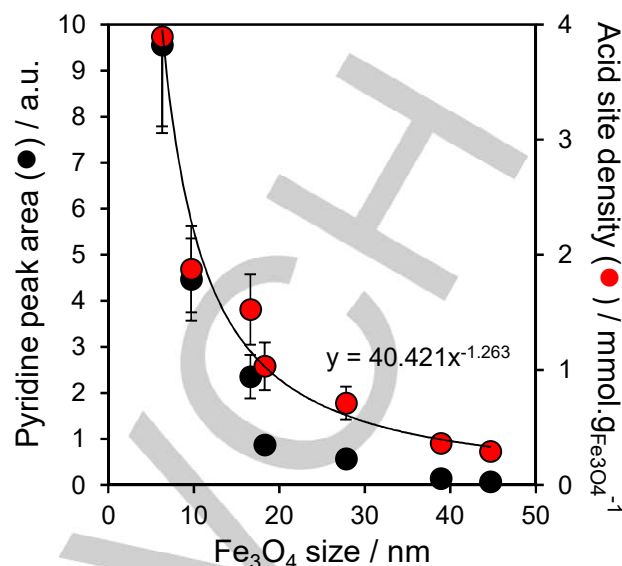

Figure 3. Surface acidity of Fe_3O_4/SiO_2 as a function of particle size. Lewis acid (1445 cm^{-1}) band intensities following pyridine titration, and acid densities derived from reactively-formed propene desorption following propylamine titration, are shown normalized to the mass of Fe_3O_4 in each sample.

of all Fe_3O_4/SiO_2 catalysts. All three X-ray methods thus confirmed the synthesis of a family of (almost) pure Fe_3O_4 nanoparticles dispersed over silica with systematically increasing sizes.

Ketonization is widely believed to proceed through adsorption of carboxylate anions at acid sites,[6b] hence the acid properties of Fe_3O_4/SiO_2 materials were was probed by pyridine titration. Resulting DRIFT spectra (Figure S5) only exhibited vibrational bands attributable to pyridine coordinated to Lewis acid sites at 1447 and 1599 cm^{-1}[39] for all Fe_3O_4 particle sizes, with band intensities inversely proportional to size (loading), indicating that small particles possess higher acidity. Figure 3 confirms that the surface acid density of supported Fe_3O_4 nanoparticles, derived from independent qualitative pyridine (DRIFTS) and quantitative propylamine (TPRS, shown in Figure S6) titrations, normalized per mass of Fe_3O_4, was inversely proportional to particle diameter, with a proportionality constant close to unity. This suggests that the acidity of our Fe_3O_4/SiO_2 materials is dictated predominantly by the geometric surface area of the iron oxide, reflecting their common pure Lewis character, and structural and electronic properties observed from XRD, XAS and XPS. The acid densities for Fe_3O_4/SiO_2 in Figure 3 compare very favourably with that of bulk magnetite (0.01-0.02 $mmol.g^{-1}$.[40]) and similar to those for Fe_2O_3 supported on mesoporous silica[41] and mesoporous ZSM-5[42] of 1.28-10.4 and 1.3-11 $mmol.g_{FeOx}^{-1}$ respectively. Some evidence for a slight increase in acid strength with particle size is apparent from a small decrease in the desorption temperature for reactively-formed propene at ~400 °C evolved following propylamine adsorption (Figure S6), which is characteristic of weak/moderate strength acid sites.

Acetic acid adsorption over Fe_3O_4/SiO_2 was explored subsequently by DRIFTS to investigate the nature and strength of resultant adsorbed acetate (Figure S7). Samples were pre-saturated with acetic acid and heated to remove physisorbed species. Spectra with bands at 1535, 1445 and 1350 cm⁻¹, characteristic of respective $\nu_{as}(COO^-)$, $\nu_{sym}(COO^-)$ and $\delta_s(CH_3)$ modes of bidentate acetate groups adsorbed over metal oxides, were observed for all Fe_3O_4 particle sizes. The frequency difference of 90 cm⁻¹ between $\nu_{as}(COO^-)$ and $\nu_{sym}(COO^-)$ stretches is indicative of a bidentate chelating carboxylate geometry,[43] which contrasts to that reported for acetic acid over ZrO_2 and TiO_2[44] wherein a bidentate bridging geometry appears favored. Acetate vibrational band intensities were proportional to the Fe_3O_4 surface area. TGA-MS of the same acetic acid saturated Fe_3O_4/SiO_2 samples revealed coincident, reaction-rate limited desorption of reactively-formed acetone and CO_2 (Figure 4), alongside competitive acetic acid desorption. Desorption temperatures and associated apparent activation energies for the evolution of reactively-formed acetone and CO_2 were independent of Fe_3O_4 particle size, the latter yielding a value of approximately 120 kJ.mol⁻¹ consistent with that obtained from continuous flow ketonisation as described below, implicating a common active site. Note that a 1:1 molar stoichiometry of acetone:CO2 products is expected, close to the observed ratio from TGA-MS in Figure 4 when the higher electron-impact ionization cross-section of acetone (~2.5 times that of CO_2 at 100 eV) is taken into account.
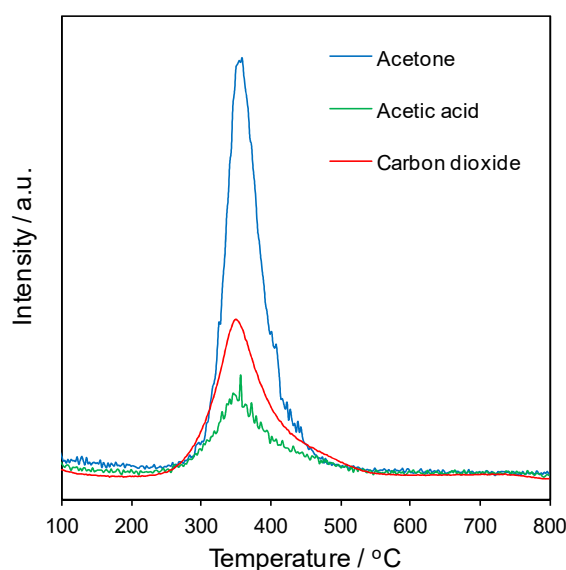

Figure 4. Temperature-programmed reaction spectra from acetic acid saturated 4 wt% Fe_3O_4/SiO_2 showing coincident evolution of ketonisation products acetone (m/z 58) and CO_2 (m/z 44).

The catalytic performance of Fe_3O_4/SiO_2 materials was evaluated in the continuous flow ketonization of acetic acid, the major acid component of fast pyrolysis oil, which requires upgrading to lower the oxygen content and improve bio-oil stability.[3, 45] Typical literature reaction temperatures of between 300-450 °C afforded steady state acetic acid conversions of 30-95 % (Figure S8) with both conversion and steady state activity (Figure S9) increasing with temperature but inversely proportional to Fe_3O_4 particle size. Apparent activation energies (calculated for acetic acid conversion <50 % in all cases) were size-invariant and 100-116 kJ.mol⁻¹ (Figure S10) consistent with literature values for continuous acetic acid ketonization over iron oxides (101 kJ.mol⁻¹[9] and 65-140 kJ.mol⁻¹[23b] over γ-Fe_2O_3) and related metal oxides (117 kJ.mol⁻¹ for ZrO_2,[25b] 78-161 kJ.mol⁻¹ over CeO_2[46] and 160 kJ.mol⁻¹ for Ru/TiO_2[47]). Corresponding rates of acetic acid conversion and acetone production, normalized to Fe_3O_4 mass, compared in Figure 5 at 400 °C confirm the superior reactivity of small Fe_3O_4 nanoparticles, in agreement with their higher mass normalised acid site density seen in Figure 3. It is interesting to note that the rates of acetic acid conversion/acetone production over an industrial Red Mud waste sample lie approximately in the middle of values for Fe_3O_4/SiO_2, indicating that Fe_3O_4 likely represents the principal active component of Red Mud. (Note that our Red Mud sample contained 25-40 nm Fe_3O_4 nanoparticles following 450 °C ketonization).
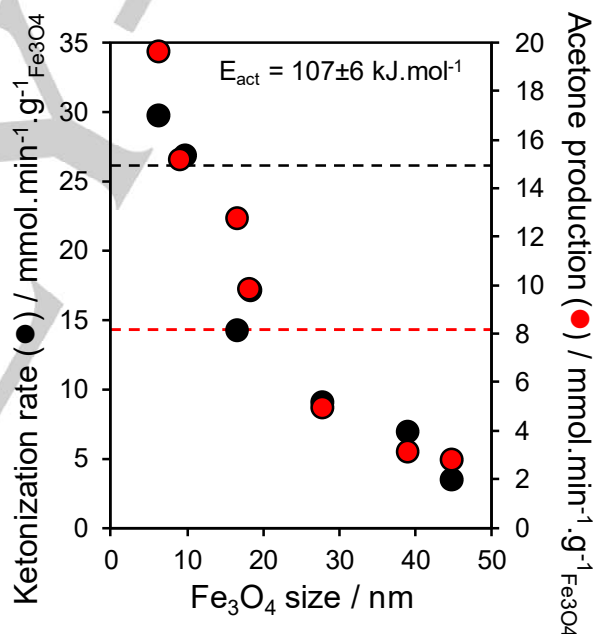

Figure 5. Mass normalized rates of acetic acid ketonization and acetone production as a function of particle size at 400 °C. Dashed lines indicate corresponding rates for Red Mud.

Direct comparison of our Fe_3O_4/SiO_2 ketonization activity with literature metal oxide catalysts is hindered by the wide range of reactor designs and operating conditions employed, and a general focus on acetic acid conversion rather than activity. However, the present acetic acid ketonization rates of 1.2-4.8 mmol.min⁻¹.g$_{catalyst}$⁻¹ (the maximum value being for 18.3 wt% Fe_3O_4/SiO_2) compare favourably with values of ~0.5 mmol.min⁻¹.g$_{catalyst}$⁻¹ reported for 5 wt% Ru/TiO2[47] in flow, and 0.2-2.4 mmol.min⁻¹.g$_{catalyst}$⁻¹ for CeO_2 catalysts in batch,[46] although a rate of 100 mmol.min⁻¹.g$_{catalyst}$⁻¹ has been claimed over strong base sites in polycrystalline pure magnesia under

flow.[48] Additional XRD of spent reference α-Fe_2O_3, γ-Fe_2O_3 and FeO phases following acetic acid ketonisation under our reaction conditions reveal their respective in situ reduction or oxidation to Fe_3O_4 (Figure S12), indicating these other iron oxide phases are simply precursors to a common magnetite active phase. Acetone does not strongly adsorb on magnetite, as evidenced by temperature programmed DRIFTS studies of the acetone-saturated oxide (Figure S13) wherein no characteristic acetone bands were visible >50 °C, and hence is expected to rapidly desorbed upon formation at 400 °C. While acetone oxidation may be possible at high temperature over iron oxides,[49] such chemistry is not expected in the present study wherein ketonisation was performed employing N_2 as the carrier gas.
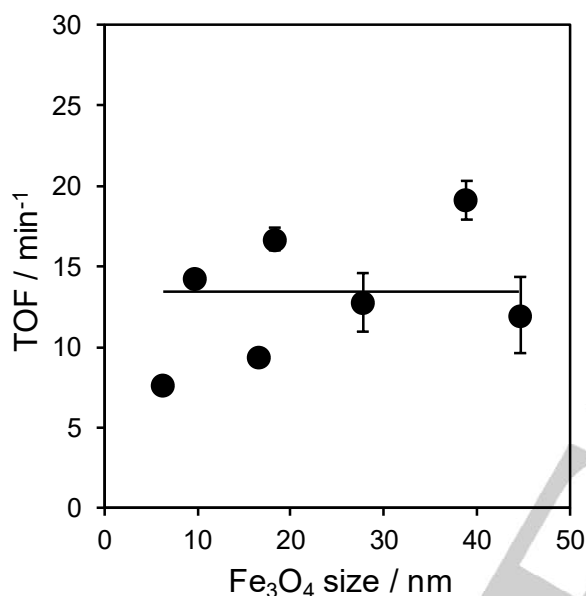

Figure 6. Turnover frequencies per acid sites for acetic acid ketonization over Fe_3O_4/SiO_2 as a function of particle size at 400 °C.

Turnover frequencies (TOFs) per surface acid site are shown in Figure 6, and reveal that acetic acid ketonization is structure-insensitive over Fe_3O_4 for nanoparticles spanning 6-60 nm, as anticipated in light of their size-invariant acid strength/character and common activation energy for ketonization. The TOF of ~13 min^{-1} is in excellent agreement with that of Red Mud of 11.9 min^{-1}, and sits in the mid-region of those reported for for continuous vapour phase propanoic acid ketonization over silica and heteropolyacid supported Pd, Pt and Cu nanoparticles of 1.3 to 34 min^{-1} reported by Alotaibi et al[50] (although these values appear to have been determing under H_2 and hence likely reflect HDO performance), and lower than those for the cross ketonization of acetic and hexanoic acid over zeolites (50 -100 min^{-1}).[51] There are few literature studies on particle size effects in carboxylic acid ketonization over oxide catalysts. For acetic acid ketonization over nanocrystalline ceria, larger particles formed via high temperature calcination deliver higher activities but lower acetone yields, however ceria crystallinity and not morphology was identified as the key

factor.[46] Propanoic acid ketonization over nanocrystalline ceria is reportedly favored over CeO_2(111) facets, dominant on larger particles, and hence also structure sensitive, although propanal and 1-propanol ketonization were structure-insensitive over the same materials. The origin of this differing reactivity between Fe_3O_4 and ceria active phases requires further investigations.

Acetone selectivity determined under differential conditions was also size-invariant at ~60 % for all Fe_3O_4/SiO_2 catalysts (Figure S11), implicating a common active (Lewis acid) site, and comparable to that reported over diverse metal oxides including those of cerium, iron, manganese, titania, vanadium and zirconium.[8-9, 48, 52]. Common side-products such as carbon monoxide, isobutene and acetaldehyde were not observed in this work, with only trace (<1 %) methane (as a primary product of acetic acid decarboxylation[8a, 53]) detected alongside acetone, CO_2 and water. Some coking was also observed, with the used catalysts containing ~5 wt.% carbon as determined by elemental CHNS analysis. All catalysts were stable at each reaction temperature for 1 h, and indeed exhibited minimal change in either conversion or selectivity upon holding for 8 h at the final 450 °C reaction temperature, however extended ageing and recylcing test are the subject of future studies.

Conclusions

Wet impregnation offers a simple means to prepare magnetite (Fe_3O_4) nanoparticles of varying size dispersed over fumed SiO_2 Physicochemical properties of such silica supported Fe_3O_4 nanoparticles are largely size-invariant, characterised by weak/moderate strength Lewis acid sites which bind acetic acid in a bidentate, chelating acetate mode. Small Fe_3O_4 nanoparticles (~6 nm diameter) afford high acid site densities as a result of their high dispersion, and exhibit excellent conversion and mass normalized specific activities for vapor phase acetic ketonization to acetone at reaction temperature between 300-450 °C. Ketonization is structure-insensitive over silica supported Fe_3O_4, which exhibits a catalytic performance comparable to that of industrial Red Mud; nanoparticulate Fe_3O_4 appears the principal active component of Red Mud waste for acetic acid ketonization, paving the way to a deeper understanding of the catalytic properties and wider application of this abundant waste material.

Experimental Section

Materials. Silica supported magnetite particles of varying sizes were prepared by wet impregnation of fumed silica with iron nitrate. Briefly, a suspension of fumed SiO_2 (supplier/code number) was stirred in EtOH at 40 °C for 30 min before addition of an appropriate volume of an ethanolic of $Fe(NO_3)_3$.$9H_2O$ solution to achieve iron loadings spanning 4-63 wt%. The slurry was stirred and evaporated to dryness at 50 °C, and the resulting solid dried at 80 °C, ground to a fine powder (60 mesh) and calcined in air in a muffle furnace at 400 °C for 2 h. The resulting orange powder was subsequently reduced in a tube furnace under flowing H_2 (10 ml.min^{-1}) at 350 °C for 30 min to obtain the desired Fe_3O_4 phase (as a grey/black powder).

Catalyst characterization. Nitrogen physisorption was performed on a Quantachrome Nova 1200 porosimeter, with samples degassed at 120 °C in vacuo for 4 h prior to recording adsorption/desorption isotherms, and surface areas determined by multipoint Brunauer-Emmett-Teller (BET) analysis. Power X-ray diffraction (XRD) patterns were collected on a Bruker D8 Advance fitted with a LynxEYE high speed strip detector and Cu K_α (1.54 Å) radiation, and a 0.2 mm Ni filter to remove K_β radiation. Crystallite sizes were estimated by peakwidth analysis using the Scherrer equation. X-ray photoelectron spectroscopy (XPS) was undertaken on a Kratos Axis HSi spectrometer fitted with a charge neutralizer and magnetic focusing lens, employing Al K_α monochromatic radiation (1486.7 eV). Spectral fitting was performed using CasaXPS version 2.3.14. Binding energies were corrected to the C 1s peak at 284.6 eV and surface atomic compositions calculated via correction for the appropriate instrument response factors. In situ XRD pattern were obtained using an Anton Parr XK900 cell interfaced to back-pressure regulated Bronkhorst ELFLOW mass flow controllers. Diffuse Reflectance Infrared Fourier Transform Spectroscopy (DRIFTS) was performed on a Nicolet iS50 FTIR spectrometer using a Harrick Scientific Praying Mantis High Temperature Reaction Chambers and associated temperature controller. Acid character was evaluated through pyridine chemisorption. Iron oxide samples were wet with pyridine (~0.2 ml) and dried in a vacuum oven at 40 °C overnight, prior to dilution to 10 wt% in dry KBr and spectra recorded in vacuo at 50 °C. Acetic acid adsorption was probed through room temperature pre-saturation (~0.2 ml) and subsequent evaporation to dryness in vacuo at 40 °C overnight. Samples were diluted to 10 wt% in dry KBr, and their spectra recorded in vacuo between 50 and 400 °C; spectra of the untreated iron oxide samples diluted to 10 wt% in dry KBr were used to perform a background subtraction and obtain the adsorbate bands. Temperature-programmed reaction spectroscopy (TPRS) of propylamine-saturated samples was employed to calculate acid site densities using a Mettler Toledo TGA/DSC2 STARe system. Catalyst samples were pre-saturated with propylamine (~0.2 ml) at room temperature and evaporated to dryness in vacuo at 40 °C overnight. Samples (~15 mg) were then heated in the TGA furnace to 800 °C at 10 °C.min^{-1} under flowing N_2 (40 ml.min^{-1}), with evolved gases analyzed by a Pfeiffer Vacuum Thermostar mass spectrometer to monitor the appearance of reactively-formed propene over acid sites. The resulting temperature-programmed desorption spectra were background corrected for contributions from physisorbed propylamine on the silica support. TEM was acquired on a JEOL 2010 microscope operated at 200 kV. Images were collected using a Gatan Ultrascan 4000 digital camera. Samples were dispersed in ethanol and deposited on 300-mesh carbon-supported copper grids and dried in air. Particle diameters were measured with ImageJ software and size distributions are based on the analysis of ~150 particles for each sample. The bulk iron content was determined by ICP-AES with a Thermo iCAP 7000 ICP-OES instrument. Fe K-edge transmission X-ray absorption spectroscopy (XAS) was performed at the XAFS beamline of the Elettra synchrotron with a Si(111) double-crystal monochromator and ring operation at 250 mA/2 GeV.

Ketonization. Catalytic ketonization of acetic acid was performed in a continuous flow, packed bed microreactor with online GC analysis. The reactor comprised a 1 cm o.d. quartz tube, within which the catalyst bed was placed centrally and retained by quartz wool plugs. A constant catalyst bed volume of 4 cm^3 was used in all experiments, comprising approximately 50 mg of each Fe_3O_4/SiO_2 diluted with fused silica granules. The reactor tube was positioned in a temperature-programmable furnace with a thermocouple placed in contact with the catalyst bed. Acetic acid was fed in a downflow fashion into the reactor using an Agilent 1260 Infinity Isocratic Pump and N_2 nitrogen carrier gas (50 ml.min^{-1}) supplied by a Brooks mass flow controller. All reactor lines were heated to 130 °C to prevent condensation, and a 1 cm diameter

metal tube packed with fused silica granules used to ensure acetic acid vaporization prior to the reactor. Product stream analysis employed a Varian 3800 GC with heated gas-sampling valve, and a BR-Q PLOT column (30 m x 0.53 mm i.d.) with a N_2 carrier. Acetone, acetic acid and methane were detected by FID and CO_2 by TCD.

[1]   a) A. V. Bridgwater, *Biomass Bioenerg.* **2012**, *38*, 68-94; b) W. N. R. W. Isahak, M. W. M. Hisham, M. A. Yarmo, T.-y. Yun Hin, *Renew. Sustainable Energy Rev.* **2012**, *16*, 5910-5923.
[2]   a) M. Patel, A. Kumar, *Renew. Sustainable Energy Rev.* **2016**, *58*, 1293-1307; b) A. R. K. Gollakota, M. Reddy, M. D. Subramanyam, N. Kishore, *Renew. Sustainable Energy Rev.* **2016**, *58*, 1543-1568.
[3]   L. Ciddor, J. A. Bennett, J. A. Hunns, K. Wilson, A. F. Lee, *J. Chem. Tech. Biotech.* **2015**, *90*, 780-795.
[4]   R. W. Snell, E. Combs, B. H. Shanks, *Top. Catal.* **2010**, *53*, 1248-1253.
[5]   A. H. Zacher, M. V. Olarte, D. M. Santosa, D. C. Elliott, S. B. Jones, *Green Chem.* **2014**, *16*, 491-515.
[6]   a) M. Renz, *Eur. J. Org. Chem.* **2005**, *2005*, 979-988; b) T. N. Pham, T. Sooknoi, S. P. Crossley, D. E. Resasco, *ACS Catal.* **2013**, *3*, 2456-2473.
[7]   J. C. Manayil, C. V. M. Inocencio, A. F. Lee, K. Wilson, *Green Chem.* **2016**, *18*, 1387-1394.
[8]   a) M. Gliński, J. Kijeński, A. Jakubowski, *Appl. Catal. A* **1995**, *128*, 209-217; b) R. Pestman, A. van Duijne, J. A. Z. Pieterse, V. Ponec, *J. Molec. Catal A* **1995**, *103*, 175-180.
[9]   A. A. Taimoor, A. Favre-Réguillon, L. Vanoye, I. Pitault, *Catal. Sci. Technol.* **2012**, *2*, 359.
[10]   G. Power, M. Gräfe, C. Klauber, *Hydrometallurgy* **2011**, *108*, 33-45.
[11]   aC. Klauber, M. Gräfe, G. Power, *Hydrometallurgy* **2011**, *108*, 11-32; bS. K. Ritter, in *C&EN News, Vol. 92*, American Chemical Society, **2014**, pp. 33-35.
[12]   E. P. Manfroi, M. Cheriaf, J. C. Rocha, *Constr. Build. Mater.* **2014**, *67, Part A*, 29-36.
[13]   R. Lu, Y. Zhang, F. Zhou, X. Wang, Q. An, Z. Meng, *Desalin. Water Treat.* **2013**, *52*, 7645-7653.
[14]   X. Ke, S. A. Bernal, N. Ye, J. L. Provis, J. Yang, J. Biernacki, *J. Am. Ceram. Soc.* **2015**, *98*, 5-11.
[15]   C. Belviso, E. Agostinelli, S. Belviso, F. Cavalcante, S. Pascucci, D. Peddis, G. Varvaro, S. Fiore, *Micropor. Mesopor. Mat.* **2015**, *202*, 208-216.
[16]   I. F. Teixeira, T. P. V. Medeiros, P. E. Freitas, M. G. Rosmaninho, J. D. Ardisson, R. M. Lago, *Fuel* **2014**, *124*, 7-13.
[17]   Q. Liu, R. Xin, C. Li, C. Xu, J. Yang, *J. Environ. Sci.* **2013**, *25*, 823-829.
[18]   a) A. López, I. de Marco, B. M. Caballero, M. F. Laresgoiti, A. Adrados, A. Aranzabal, *Appl. Catal. B* **2011**, *104*, 211-219; b) A. Veses, M. Aznar, J. M. López, M. S. Callén, R. Murillo, T. García, *Fuel* **2015**, *141*, 17-22.
[19]   S. Sushil, V. S. Batra, *Appl. Catal. B* **2008**, *81*, 64-77.
[20]   M. Balakrishnan, V. S. Batra, J. S. J. Hargreaves, A. Monaghan, I. D. Pulford, J. L. Rico, S. Sushil, *Green Chem.* **2009**, *11*, 42.
[21]   E. Karimi, A. Gomez, S. W. Kycia, M. Schlaf, *Energy Fuels* **2010**, *24*, 2747-2757.
[22]   a) E. Karimi, I. F. Teixeira, L. P. Ribeiro, A. Gomez, R. M. Lago, G. Penner, S. W. Kycia, M. Schlaf, *Catal. Today* **2012**, *190*, 73-88; b) W. Hajjaji, S. Andrejkovičová, C. Zanelli, M. Alshaaer, M. Dondi, J. A. Labrincha, F. Rocha, *Mater. Des.* **2013**, *52*, 648-654.
[23]   a) S. S. Jewur, J. C. Kuriacose, *J. Res. Inst. Catalysis, Hokkaido Univ* **1976**, *24*, 73-82; b) J. C. Kuriacose, S. S. Jewur, *J. Catal.* **1977**, *50*, 330-341.
[24]   a) A. Pulido, B. Oliver-Tomas, M. Renz, M. Boronat, A. Corma, *ChemSusChem* **2013**, *6*, 141-151; b) A. V. Ignatchenko, J. S. DeRaddo, V. J. Marino, A. Mercado, *Appl. Catal. A* **2015**, *498*, 10-24.
[25]   a) O. Nagashima, S. Sato, R. Takahashi, T. Sodesawa, *J. Molec. Catal. A* **2005**, *227*, 231-239; b) A. V. Ignatchenko, E. I. Kozliak, *ACS Catal.* **2012**, *2*, 1555-1562; c) R. Pestman, R. M. Koster, A. van Duijne, J. A. Z. Pieterse, V. Ponec, *J. Catal.* **1997**, *168*, 265-272.

[26] A. V. Ignatchenko, *J. Phys. Chem. C* **2011**, *115*, 16012-16018.
[27] T. S. Hendren, K. M. Dooley, *Catal. Today* **2003**, *85*, 333-351.
[28] F. Gonzalez, G. Munuera, J. A. Prieto, *J. Chem. Soc., Faraday Trans. 1* **1978**, *74*, 1517-1529.
[29] T. N. Pham, D. Shi, D. E. Resasco, *Top. Catal.* **2013**, *57*, 706-714.
[30] L. Wang, D. Su, L. Jiang, X. Feng, *Soft Mater.* **2014**, *12*, 306-314.
[31] Y. F. Krupyanskii, I. P. Suzdalev, *J. Phys. Colloques* **1974**, *35*, C6-407-C406-410.
[32] K. Parekh, R. V. Upadhyay, R. V. Mehta, *Hyperfine Interact.* **2005**, *160*, 211-217.
[33] K. C. Nam, K.-H. Choi, K.-D. Lee, J. H. Kim, J.-S. Jung, B. J. Park, *J. Nanomater.* **2016**, *2016*, 1-9.
[34] V. M. Gun'ko, I. F. Mironyuk, V. I. Zarko, E. F. Voronin, V. V. Turov, E. M. Pakhlov, E. V. Goncharuk, Y. M. Nychiporuk, N. N. Vlasova, P. P. Gorbik, O. A. Mishchuk, A. A. Chuiko, T. V. Kulik, B. B. Palyanytsya, S. V. Pakhovchishin, J. Skubiszewska-Zieba, W. Janusz, A. V. Turov, R. Leboda, *Journal of colloid and interface science* **2005**, *289*, 427-445.
[35] a) H. Okudera, A. Yoshiasa, K.-i. Murai, M. Okube, T. Takeda, S. Kikkawa, *JMPS* **2012**, *107*, 127-132; b) G. A. Waychunas, M. J. Apted, G. E. Brown, *Phys. Chem. Miner.* **1983**, *10*, 1-9.
[36] a) M. Benfatto, J. A. Solera, J. n. García Ruiz, J. Chaboy, *Chem. Phys.* **2002**, *282*, 441-450; b) A. Espinosa, A. Serrano, A. Llavona, J. Jimenez de la Morena, M. Abuin, A. Figuerola, T. Pellegrino, J. F. Fernández, M. Garcia-Hernandez, G. R. Castro, M. A. Garcia, *Meas. Sci. Technol.* **2012**, *23*, 015602.
[37] a) R. P. Gupta, S. K. Sen, *Phys. Rev. B* **1975**, *12*, 15-19; b) N. S. McIntyre, D. G. Zetaruk, *Anal. Chem.* **1977**, *49*, 1521-1529.
[38] a) M. C. Biesinger, B. P. Payne, A. P. Grosvenor, L. W. M. Lau, A. R. Gerson, R. S. C. Smart, *Appl. Surf. Sci.* **2011**, *257*, 2717-2730; b) A. P. Grosvenor, B. A. Kobe, M. C. Biesinger, N. S. McIntyre, *Surf. Interface Anal.* **2004**, *36*, 1564-1574; c) T. Yamashita, P. Hayes, *Appl. Surf. Sci.* **2008**, *254*, 2441-2449; d) T. Fujii, F. M. F. de Groot, G. A. Sawatzky, F. C. Voogt, T. Hibma, K. Okada, *Phys. Rev. B* **1999**, *59*, 3195-3202.
[39] G. Busca, *Catal. Today* **1998**, *41*, 191-206.
[40] a) S. Yean, L. Cong, C. T. Yavuz, J. T. Mayo, W. W. Yu, A. T. Kan, V. L. Colvin, M. B. Tomson, *J. Mater. Sci.* **2011**, *20*, 3255-3264; b) V. Philippini, A. Naveau, H. Catalette, S. Leclercq, *J. Nucl. Mater.* **2006**, *348*, 60-69; c) X. Xue, K. Hanna, C. Despas, F. Wu, N. Deng, *J. Molec. Catal. A* **2009**, *311*, 29-35.
[41] A. Gervasini, C. Messi, P. Carniti, A. Ponti, N. Ravasio, F. Zaccheria, *J. Catal.* **2009**, *262*, 224-234.
[42] A. J. J. Koekkoek, H. Xin, Q. Yang, C. Li, E. J. M. Hensen, *Micropor. Mesopor. Mat.* **2011**, *145*, 172-181.
[43] a) N. T. Nolan, M. K. Seery, S. C. Pillai, *J. Phys. Chem. C* **2009**, *113*, 16151-16157; b) G. B. Deacon, R. J. Phillips, *Coord. Chem. Rev.* **1980**, *33*, 227-250; c) V. Zeleňák, Z. Vargová, K. Györyová, *Spectrochim. Acta Mol. Biomol. Spectrosc.* **2007**, *66*, 262-272; d) J. Simon-Kutscher, A. Gericke, H. Hühnerfuss, *Langmuir* **1996**, *12*, 1027-1034.
[44] G. Pacchioni, *ACS Catal.* **2014**, *4*, 2874-2888.
[45] a) C. A. Mullen, A. A. Boateng, *Energy Fuels* **2008**, *22*, 2104-2109; b) A. V. Bridgwater, S. Czernik, J. Diebold, J. C. Meier, A. Oasma, G. V. C. Peacocke, J. Pizkorz, D. Radlein, *Fast Pyrolysis of Biomass: A Handbook*, CPL Press, Newbury Berkshire, UK, **1999**.
[46] R. W. Snell, B. H. Shanks, *Appl. Catal. A* **2013**, *451*, 86-93.
[47] T. N. Pham, D. Shi, D. E. Resasco, *J. Catal.* **2014**, *314*, 149-158.
[48] G. Mekhemer, S. Halawy, M. Mohamed, M. Zaki, *J. Catal.* **2005**, *230*, 109-122.
[49] Y. Xia, H. Dai, H. Jiang, L. Zhang, J. Deng, Y. Liu, *Journal of Hazardous Materials* **2011**, *186*, 84-91.
[50] M. A. Alotaibi, E. F. Kozhevnikova, I. V. Kozhevnikov, *Appl. Catal. A* **2012**, *447-448*, 32-40.
[51] M. Godavarthy, University of Oklahoma **2016**.
[52] K. M. Parida, A. Samal, N. N. Das, *Appl. Catal. A* **1998**, *166*, 201-205.
[53] a) R. A. L. Baylon, J. Sun, K. J. Martin, P. Venkitasubramanian, Y. Wang, *Chem. Commun.* **2016**, *52*, 4975-4978; b) M. A. Hasan, M. I. Zaki, L. Pasupulety, *Appl. Catal. A* **2003**, *243*, 81-92.

Entry for the Table of Contents

FULL PAPER

Silica supported Fe_3O_4 nanoparticles are an abundant, low cost catalyst for the upgrading of fast pyrolysis bio-oils to produce green transport fuels through acetic acid ketonization. Lewis acids sites arising from nanoparticulate Fe_3O_4 are likely the active site responsible for ketonization within Red Mud waste.
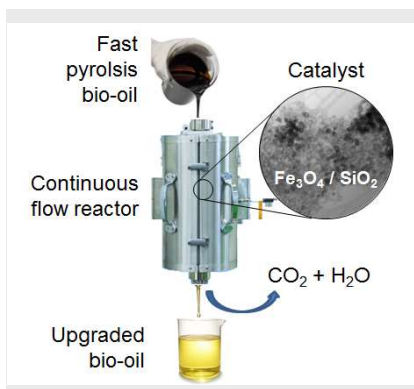
Author(s), Corresponding Author(s)*

Page No. – Page No.

Title